

Ion diffusion overestimates figures of merit in polymeric mixed conductors

Received: 13 February 2025

Accepted: 3 December 2025

Published online: 27 January 2026



Maryam Shahi ^{1,2}, Vianna N. Le^{1,2}, Paula Alarcon Espejo ^{1,2}, Bowen Ding^{3,4}, Joel H. Bombile ^{2,5}, Chad Risko ^{2,5}, Martin Heeney ^{3,4,6} & Alexandra F. Paterson ^{1,2,7}

Figures of merit are used to translate science to technology. For organic mixed ionic–electronic conductors (OMIECs), the product of mobility and volumetric capacitance, i.e., the μC^* product, is the figure of merit used to guide the development of technologies ranging from bioelectronics to neuromorphics. While organic electrochemical transistors (OECTs) are used extensively to measure the μC^* product, if there is a kink in the transistor current, then the μC^* product is overestimated. Here, we show that the origin of the kink is a change in the rate with which the ions diffuse into the channel. We also discover that the OECT channel geometry has an unprecedented role on how the ions are distributed within the OMIEC. Finally, we observe that electronic charge carriers are first be injected and drift in the OMIEC, before ions can drift from the electrolyte into the OMIEC. Overall, the diverse charge transport phenomena identified here are essential for understanding the complexities of integrating novel OMIECs into traditional device structures, providing the key information needed to realize their promising application potential.

Organic electrochemical transistors (OECTs) transport ions and electrons through organic mixed ionic electronic conductors (OMIECs) that are mechanically flexible^{1–3} and can be processed from solution, over large areas using low-cost printing techniques^{4–6}. While the 2007 Bernards and Malliaras model has enabled OECTs to be used as the primary tool for measuring figures of merit (FOM) that benchmark and compare OMIEC materials, recent reports highlight significant differences between measured and predicted data^{7–12} that arise from, for example, laterally flowing ions⁸, counterions⁹, and exponential carrier concentration/conductance^{10–12}, all of which are unaccounted for in the model. A key consequence of the discrepancies between measured and predicted data are overestimated FOM^{13,14}. Specifically, mobility (μ) and the μC^* product (where C^* is the volumetric capacitance) were recently shown to be overestimated by the Bernards and Malliaras model⁷, when an unpredicted, non-linear feature or “kink” is present in the square root of the OECT saturation drain current ($\sqrt{I_D}$). The latter is important because

the kink in $\sqrt{I_D}$ is a general problem throughout the diverse catalog of OECT systems, including electron- and hole-transporting OECTs, and OECTs operating with different electrolytes (Fig. S1). For organic thin-film transistors (OTFTs), the kink is caused by a sharp change in contact resistance when the transistor switches on¹⁵. For OECTs, while channel resistance has been found to play a key role in discrepancies between measured and predicted data^{7,16}, the exact mechanism underpinning the kink in $\sqrt{I_D}$ remains unknown. Identifying the physical origin of the kink—the feature that acts as a clear indication or signature that μ and the μC^* product are overestimated—is essential for establishing models and measurements that reliably report OMIEC FOM, for applications spanning thermoelectrics, photocatalysts, energy storage, neuromorphic computing, and bioelectronics¹⁷.

Here, elucidating the origin of the signature kink uncovers further important charge transport phenomena. First, we find that the kink originates from a change in the rate with which ions diffuse into the channel,

¹Department of Chemical and Materials Engineering, University of Kentucky, Lexington, KY, USA. ²Centre for Applied Energy Research, University of Kentucky, Lexington, KY, USA. ³Department of Chemistry and Centre for Processable Electronics, Imperial College London, London, UK. ⁴Molecular Sciences Research Hub (White City Campus), London, UK. ⁵Department of Chemistry, University of Kentucky, Lexington, KY, USA. ⁶Physical Sciences and Engineering Division (PSE), King Abdullah University of Science and Technology (KAUST), Thuwal, Saudi Arabia. ⁷Department of Electrical Engineering, University of Kentucky, Lexington, KY, USA. ✉e-mail: alexandra.paterson@uky.edu

and explain this phenomenon using Fick's second law of diffusion, along with the formation of a hard gap in the density of states (DOS) from increased Coulombic interactions causing carrier localization. Second, we discover that OECT channel geometry plays a significant yet unexpected role in determining the location of the conductive channel: If the channel length is small, the conductive channel forms closer to the OMIEC/electrolyte interphase, whereas the conductive channel is better distributed through the bulk when the channel length is large. The latter parasitic channel effects are further confirmed by finding that the material property, diffusion coefficient, is a function of channel length. Third, the system investigated herein suggests electronic carrier injection and drift happen before ionic drift, thereby offering an important contribution to a persistent OECT question: Do electronic, or ionic, charges enter the OECT channel first? Overall, identifying the mechanisms underpinning differences in predicted and measured data is anticipated to enable the development of new measurements and models that reliably report benchmark FOM, to guide OMIEC material and device development, for technologies spanning thermoelectrics, photocatalysis, energy storage, neuromorphic computing, and low-cost biosensors.

Results

A peak in the ionic conductivity correlates with an unexpected increase in activation energy

We measured the activation energy (E_A) of the OECT drain current (I_D) by thermally activating trapped charges into delocalized states, to

better understand the transport mechanisms underpinning I_D and therefore the kink in I_D . Temperature (T)-dependent measurements were used to measure E_A as a function of gate voltage (V_G), from the slope of the Arrhenius plot, for three systems with fixed electrolyte counterions and anion of varying sizes, following the relationship

$$I_D \propto \exp\left(-\frac{E_A}{k_B T}\right) \quad (1)$$

where k_B is the Boltzmann constant. Figure 1 shows E_A for accumulation mode, p-type poly[(3,6-bis(triethyleneglycolmonomethylether)thieno[3,2] thiophene-co-thiophene) (pT2gTT)⁴⁸ OECTs (Fig. S2a, b). Room temperature ionic liquid electrolytes 1-butyl-3-methylimidazolium tetrafluoroborate (BMIMBF₄⁻), 1-butyl-3-methylimidazolium trifluoromethanesulfonate (BMIMOTf⁻) and 1-butyl-3-methylimidazolium hexafluorophosphate (BMIMPF₆⁻) were selected because their anions increase in volumetric size, from BF₄⁻ (100 Å³) to PF₆⁻ (125 Å³) and OTf⁻ (154 Å³) (Figs. 1a–c and S3), they are stable liquids in the vacuum required for the temperature-dependent measurements, and because interest in ionic liquids for OMIECs and OECTs is growing^{49–21}. Figures 1d and S2d, e show that, for the smallest anion, BF₄⁻, E_A decreases continually from 270 meV at $V_G = 0$ V, to 17 meV at $V_G = -1.0$ V. In contrast, Fig. 1g, j shows an abrupt increase in E_A at $V_G = -0.45$ V and $V_G = -0.3$ V for the two larger anions, PF₆⁻ and OTf⁻, respectively. The abrupt increase in E_A for OTf⁻ and PF₆⁻ is

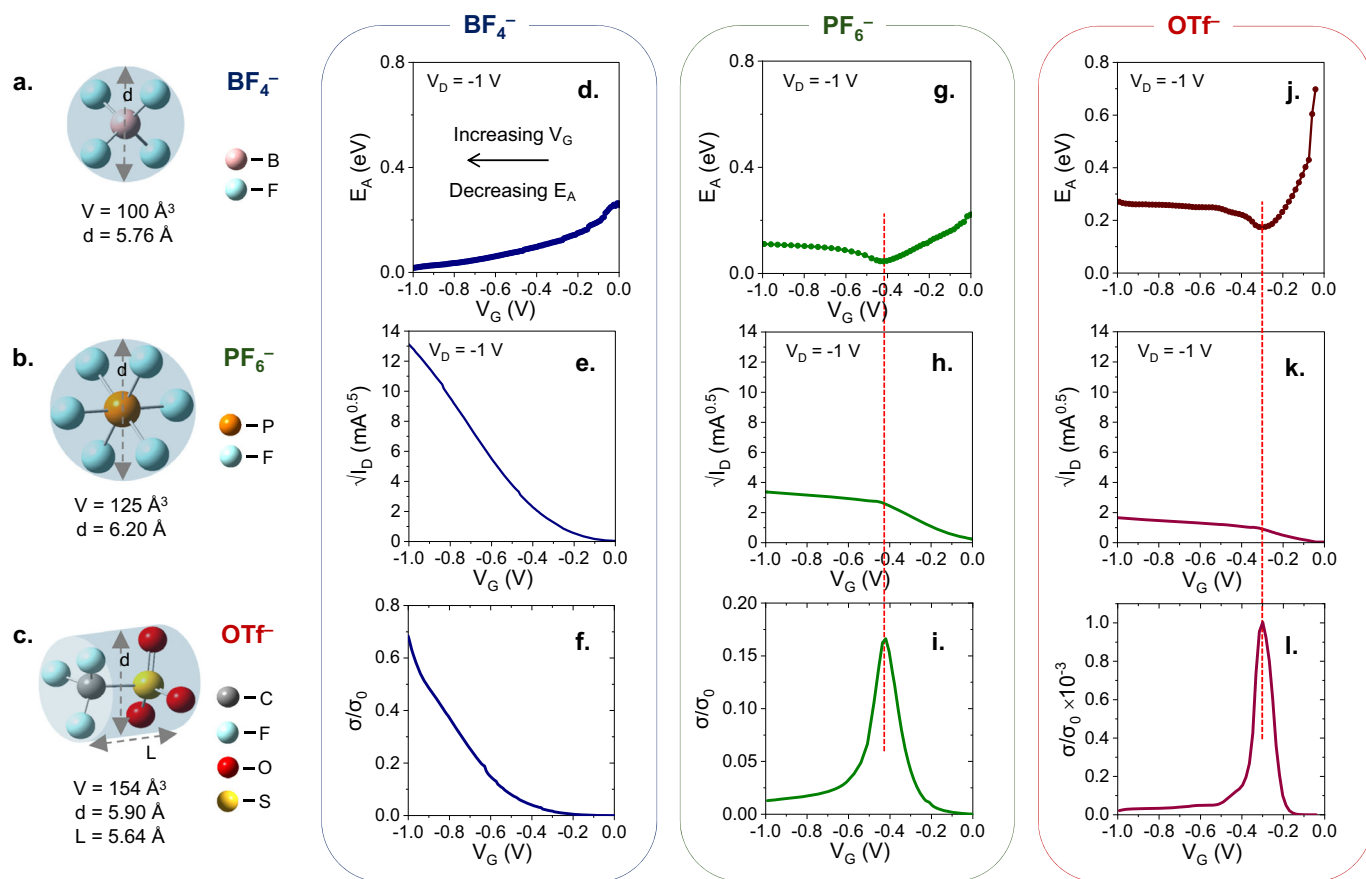


Fig. 1 | Temperature-dependent organic electrochemical transistor measurements. Density functional theory (DFT)-derived volumes for anions in room temperature ionic liquids: **a** BF₄⁻ in BMIMBF₄⁻, **b** PF₆⁻ in BMIMPF₆⁻, and **c** OTf⁻ in BMIMOTf⁻. **d** Activation energy (E_A), **e** square root of the drain current ($\sqrt{I_D}$) and **f** normalized ionic conductivity (σ/σ_0) when the ionic liquid BMIMBF₄⁻ is used as the organic electrochemical transistor (OECT) electrolyte. **g** E_A , **h** $\sqrt{I_D}$ and **i** σ/σ_0 when the ionic liquid BMIMPF₆⁻ is the OECT electrolyte. **j** E_A , **k** $\sqrt{I_D}$ and **l** σ/σ_0 when

the ionic liquid BMIMOTf⁻ is the OECT electrolyte. The dashed lines in (g–i) and (j–l) show the direct relationship between an unexpected, abrupt increase in E_A , the peak in σ/σ_0 , and kink in $\sqrt{I_D}$. Comparatively, (d–f) shows that when there is no increase in E_A , and no peak in σ/σ_0 , there is no kink in $\sqrt{I_D}$. All measurements are all carried out under vacuum with pT2gTT as the active channel material. All OECTs have 200 μm channel lengths and widths, respectively, and E_A is calculated when the drain voltage (V_D) = -1.0 V.

unexpected. Specifically, E_A is expected to continually decrease as V_G increases, because as more charges are put into the system the doping level increases to fill high energy hole sites and shift the Fermi level so that lower energy sites in the DOS can be accessed, and a more energetically and spatially uniform pathway for hole transport is created in the OMIEC²². Interestingly, Fig. 1h, k shows that the unexpected increase in E_A directly correlates with the kink in $\sqrt{I_D}$.

The origin of the kink may therefore be explained by identifying the origin of the increase in E_A . Here, E_A is the energy needed for the thermally activated transport mechanisms underpinning I_D ^{23,24}: (i) Injection across the barrier at the OMIEC/contact interface; (ii) ion transport; (iii) hole mobility^{10,25–28}. (i) can be excluded as the cause of the abrupt change in E_A , because contact resistance in electrochemical organic transistors is weakly dependent on the metal/semiconductor pair²⁹, and here the metal/semiconductor pair is identical for each OECT in Fig. 1. Therefore, the difference in contact resistance (or the energy required to inject charges across the barrier at the OMIEC/contact interface) is negligible between the three systems. Interestingly, for (ii), the Bernards and Malliaras model only considers the drift of ions in the electrolyte³⁰. However, factors including electrolyte ion concentration^{31,32}, ion mobility^{33,34}, and ion injection efficiency³⁵ impact OECT I_D and response time^{36–40}. Indeed, while the model does not consider ion diffusion, ion diffusion counteracts ions drifting within the channel as the ion concentration increases, reaching a steady state when equilibrium is established (Fig. S6)^{27,41,42}. We therefore explored whether ion diffusion impacts the increase in E_A —and the kink $\sqrt{I_D}$ —by calculating ion conductivity (σ_{ion}), which is related to the diffusion coefficient (D) by

$$D = \frac{\sigma_{ion} k_B T}{(nz)e^2} \quad (2)$$

where n is the number density, z represents the ion charge and e is the elementary charge. (See Supplementary Equations and Discussion for further details on evaluating σ_{ion} from E_A). Figures 1g–l and S4 show a peak in σ_{ion} calculated from E_A extracted from I_D , that directly correlates with the kink $\sqrt{I_D}$. Furthermore, Fig. S5 shows a peak in σ_{ion} calculated from E_A extracted from the gate current (I_G), which reflects the ionic transport/current only, also correlates with the kink $\sqrt{I_D}$. Because a peak in σ_{ion} corresponds to a maximum in the diffusivity (see Supplementary Equations and Discussion), the data therefore suggest that ion diffusion or ion mobility (where diffusivity and mobility have a linear relationship^{2,43}, and therefore a change or peak occurs at the same point) could be a possible origin of the kink.

The kink is caused by a change in the rate with which ions diffuse into the channel

To explore whether a change in ion diffusion corresponds with the kink in $\sqrt{I_D}$, we used Fick's second law of diffusion (Fig. S6), which states that the ion diffusion rate changes because of changes in the ion concentration gradient inside a material^{44,45}

$$\frac{dc}{dt} = D \frac{d^2c}{dx^2} \quad (3)$$

where c is the concentration, t is time, D is the diffusion coefficient, x is the position, $\frac{dc}{dt}$ is the rate of change in concentration, and $\frac{dc}{dx}$ is the concentration gradient which is directly proportional to the diffusion flux. In OECTs, because both drift and diffusion happen (and also happen in more than one dimension)^{8,10,12}, the Nernst–Planck drift-diffusion equation is more relevant. The Nernst–Planck equation applies an electric field to Fick's second law and accounts for ion drift, by combining drift and diffusion dynamics through²⁵

$$\frac{\partial c}{\partial t} = \nabla \cdot D \left(\nabla c + \frac{zF}{RT} c \nabla \phi \right) \quad (4)$$

where z is the ion valance, ∇c is the concentration gradient, F is the Faraday constant, R is the universal gas constant, and ϕ is the electric potential. Equation 4 is the conservation of mass for charged species, where ion drift (charge transport; the second term on the right-hand side) is intrinsically coupled to ion diffusion (mass transport; Fick's second law, the first term on the right-hand side) through c . As an electric field is applied in an OECT, the drift component moves ions into the channel, which accumulate and change the concentration of ions inside the channel. A new steady-state ($\frac{dc}{dt}$ tending towards zero) is then established by changing the diffusion term by changing the rate in which ions are diffusing into the channel. The Nernst–Planck equation therefore suggests that the electric potential gradient $\nabla \phi$ can be used to indirectly modulate the ion concentration gradient, and subsequently modulate ion diffusion rate, based on Fick's second law. In an OECT channel, assuming no interactions between charges, $\nabla \phi$ is equal to the total combination of vertical V_G combined with the lateral drain voltage (V_D).

One way to change $\nabla \phi$, and therefore ion diffusion rate, is to purposefully reduce V_D by introducing short channel effects. Briefly, when channel length (L) is small, the channel resistance is on par with the contact resistance and the voltage dropped across the channel—which is directly proportional to the ratio of R_C over the cumulative resistance of R_{CH} and R_C —is amplified⁴⁶. OECTs with short L therefore experience lower V_D , and subsequently lower effective voltage and $\nabla \phi$ in the channel⁴⁶. We therefore purposefully enhanced the lateral voltage drop between the source and the drain in pT2gTT OECTs by fixing OECT channel width (W) at 500 μm and varying L from 30 μm , 50 μm , 80 μm , 150 μm , 200 μm and 250 μm (Fig. 2a), and measured the corresponding ionic charges injected ($Q_{injected}$) into the channels as a function of V_G (Fig. 2b, c), using the displacement current method (DCM) (Fig. S7a–c)^{47,48}. We selected PF_6^- to carry out the lateral field experiments and investigate the effects of ion diffusion on the kink, because PF_6^- is a larger anion that shows the kink in I_D , has a lower freezing point and therefore broader range over which the IL remains a liquid for the temperature-dependent measurements, and has produced reliable and reproducible OECT data. Remarkably, Fig. 2d–g shows that a change in $Q_{injected}$ —and therefore a change in the rate with which ions are injected into the channel—directly correlates with a kink in $\sqrt{I_D}$, but only in the largest channel ($L = 250 \mu\text{m}$). On the other hand, within the same voltage range, there is no change in $Q_{injected}$ and therefore a constant charge injection rate for the smallest channel ($L = 30 \mu\text{m}$); furthermore, there is no kink in $\sqrt{I_D}$. The output curves in Fig. S8 further confirm the impact of the change in $Q_{injected}$ in $L = 250 \mu\text{m}$, compared to $L = 30 \mu\text{m}$, with an abrupt flattening and plateau in I_D at high V_G . Finally, we confirmed the relationship between the rate of injected ionic charges and the kink in $\sqrt{I_D}$ by increasing $\nabla \phi$ in the small channel ($L = 30 \mu\text{m}$); Fig. 2f, g and S9 show that increasing $\nabla \phi$ even further, by using a high V_G ($V_G = -2.0 \text{ V}$), indeed causes a change in $Q_{injected}$ in the small channel, by modulating the concentration gradient and diffusion rate using Fick's second law. Overall, while the kink in $\sqrt{I_D}$ is present for both the large and small channel lengths, it occurs at much higher voltages in the small channel. In each case, the change in the rate of injected ionic charges is shown to directly correspond with the kink in $\sqrt{I_D}$.

Ions dominate charge transport in the saturation regime

The data so far suggests that a change in the rate with which ions diffuse into the channel is the mechanism causing the non-linearity in $\sqrt{I_D}$, a feature which is unpredicted by the Bernards and Malliaras model, and symbolizes unreliable and overestimated μ and μC^* product values. However, it is possible that ion transport is not solely responsible for the kink. Specifically, a drop off in μ can occur in highly doped organic semiconductors when, for example, morphology becomes disrupted, or charged species such as bipolarons form^{49–51}. Additionally, a change in μ or the mobility edge could be equally

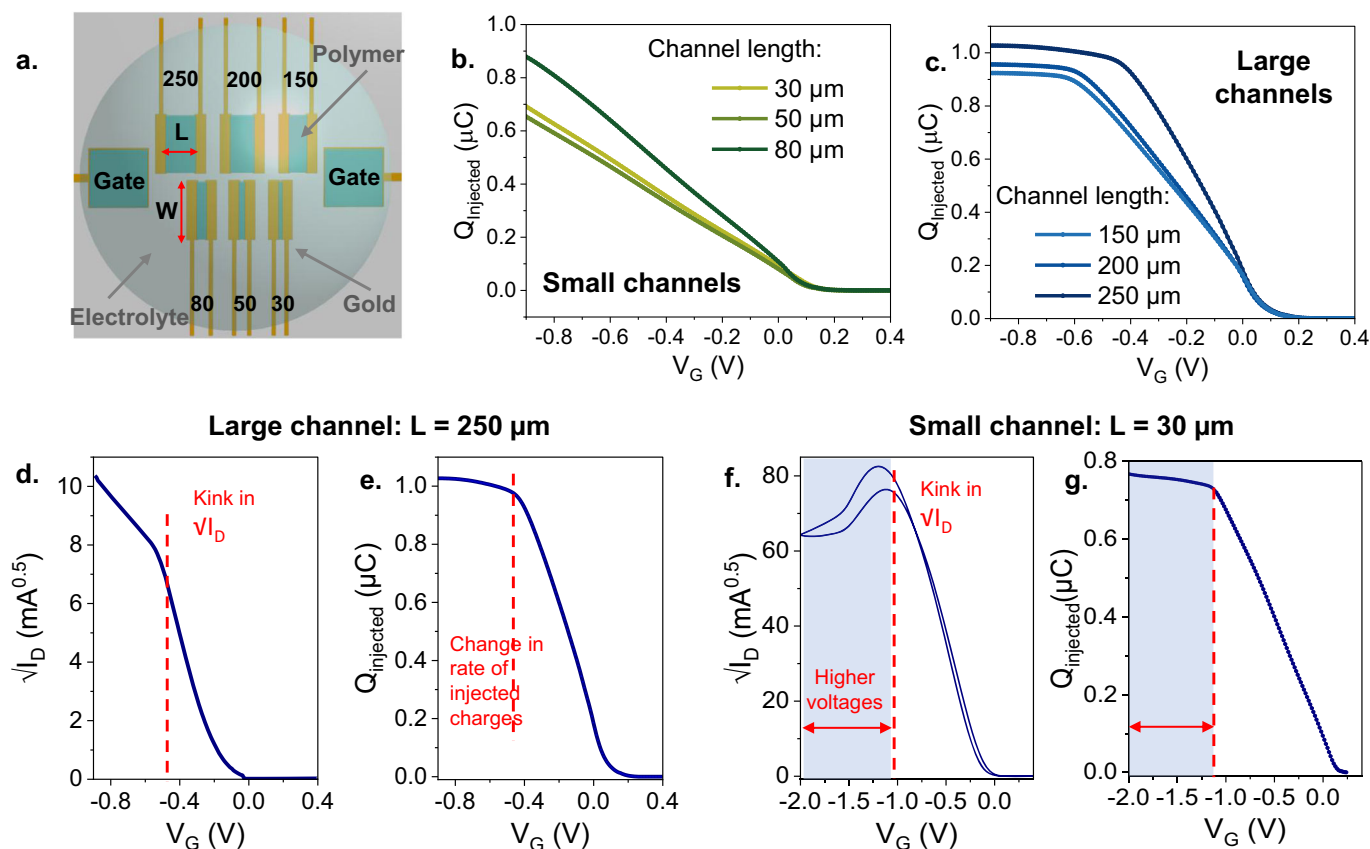


Fig. 2 | A change in ion diffusion rate causes the kink. a Schematic showing organic electrochemical transistors (OECTs) used in this article. Channel width (W) is fixed at $500 \mu\text{m}$, and length (L) is varied from $L = 30 \mu\text{m}$, $50 \mu\text{m}$, $80 \mu\text{m}$, $150 \mu\text{m}$, $200 \mu\text{m}$, and $250 \mu\text{m}$. OECTs are in bottom-contact bottom-gate configuration, with a polymer coated gold electrode as the gate electrode. **b** Ionic charge injection (Q_{injected}) as a function of gate voltage (V_G) for the smaller channels: $L = 30 \mu\text{m}$, $50 \mu\text{m}$, and $80 \mu\text{m}$. **c** Q_{injected} as a function of V_G for the larger channels: $L = 150 \mu\text{m}$, $200 \mu\text{m}$, and $250 \mu\text{m}$. The sweep rate is 11 mV/s for all data. **d** Square root of the drain current ($\sqrt{I_D}$) measured at drain voltage (V_D) = -0.9 V

for $L = 250 \mu\text{m}$. **e** Q_{injected} for $L = 250 \mu\text{m}$ measured at sweep rate 11 mV/s , with a dashed line to indicate that the kink in $\sqrt{I_D}$ directly corresponds with the change in rate of injected ionic charges. **f** $\sqrt{I_D}$ measured at $V_D = -0.9 \text{ V}$ for $L = 30 \mu\text{m}$. **g** Q_{injected} for $L = 30 \mu\text{m}$ measured at sweep rate 20 mV/s , where the difference in scan rate does not impact overall conclusion and finding (see Fig. S11). Again, the dashed line indicates that the kink in $\sqrt{I_D}$ directly corresponds with the change in rate of injected ionic charges. All measurements are all carried out under vacuum with pT2gTT as the active channel material and BMIMPF₆⁻ as the electrolyte.

responsible for the abrupt increase in E_A , because E_A is the difference in energy between the mobility edge—which separates localized and delocalized charges—and the electronic charge carrier with the greatest energy. Furthermore, our argument began with E_A extracted from I_D , which includes energy needed for the thermally activated hole μ (i.e. (iii) hole mobility). To explore the role of the voltage-dependent μ , in the context of the kink in $\sqrt{I_D}$ we used the DCM to measure μ as a function of V_G and compared the smallest ($L = 30 \mu\text{m}$) and largest ($L = 250 \mu\text{m}$) channels (Figs. 3a, b and S12). While the very clear drop off in μ at $V_G = -0.6 \text{ V}$ in the smallest channel does not correlate with either a change in saturation I_D or kink in $\sqrt{I_D}$ (Figs. 3a and S12a), the large channel shows a change in μ corresponds with a change in saturation I_D (Fig. 3b) and kink in $\sqrt{I_D}$ (Fig. S12b). In the small channel, the only change corresponding to the drop off in μ is observed in the linear regime ($V_D = -0.1 \text{ V}$, Fig. 3a), suggesting that the change in Q_{injected} dominates charge transport and I_D in the saturation regime. The latter observation may also explain why accounting for the non-linear relationship between μ and charge density, by introducing a power-law term ($\mu = \mu_0 \left(\frac{p}{p_0}\right)^a$) into the Bernards and Malliaras model, was previously unable to predict the current measured across the whole voltage range in OECTs⁵². Overall, it is the change in the rate of injected ionic charges - not the drop off in electronic charge carrier μ - that dominates the saturation regime and leads to the kink in $\sqrt{I_D}$.

While the data elucidates the origin of the kink, there is an additional observation about the order of charge transport mechanisms as an OECT is switched on. Specifically, the lateral electric field in a transistor directly controls the lateral injection and drift of charge carriers, and not the vertical drift and accumulation of the charges; for OECTs, the ions are the charges that drift in the vertical field to accumulate in the channel. It is therefore surprising that reducing the lateral field (by decreasing the channel length) has such a dramatic impact on both ion drift and diffusion, i.e., Q_{injected} , when the vertical field (V_G) is the same (Fig. 2b, c). While ion diffusion is indirectly impacted by the lateral voltage, through $\nabla\phi$, the fact that ions drifting vertically are influenced by lateral charge injection and drift, suggests that electron/hole injection and drift are a prerequisite for anions/cations to drift into the channel. We note that here we are discussing stage two out of the three stages of OECT operation, where the first stage is the off state. In the off state, while ions diffuse into the channel from the electrolyte into swollen polymers, this is not a prerequisite for electronic charge carriers to be injected into the transistor; if ion diffusion occurs before the OECT is switched on, the effects would be similar to other doped transistors, and with ion diffusion alone, the channel would behave as an Ohmic resistor (no modulation). The second operational stage is as the OECT switches on; in this article, we are describing the sequence of mechanisms for this particular polymer/electrolyte system to switch on: Electronic charge carrier injection and drift happen before ions can drift into the channel. The third stage is after the

system is switched on; recent work, for example, has shown that once the device is on, hole transport dominates the doping front propagation in accumulation polymeric electrochemical devices²². Overall, the finding here is a valuable contribution towards the debate as to whether electronic or ionic charges enter the OECT channel first, or whether both mechanisms happen simultaneously.

Channel geometry leads to either volumetric or interphase channels

A further observation from the data so far is that channel geometry appears to be another factor causing unexpected, and significant,

differences and inconsistencies between the current measured in OECTs, and the current predicted by the Bernardis and Malliaras model. To further investigate this discrepancy between measured and predicted current as a result of channel geometry, we measured D using electrochemical impedance spectroscopy (EIS). Although D is a material property and should therefore be the same value regardless of channel size, Fig. S13 indicates that D is a function of both L and V , for pT2gTT OECTs with BMIMPF₆⁻. Indeed, Fig. 3c clearly indicates “parasitic” channel effects, by showing that D changes by over an order of magnitude depending on L , with D decreasing from $1.4 \times 10^{-8} \text{ cm}^2 \text{ s}^{-1}$ for the larger channel lengths ($L = 250, 200 \mu\text{m}$, and $150 \mu\text{m}$), to

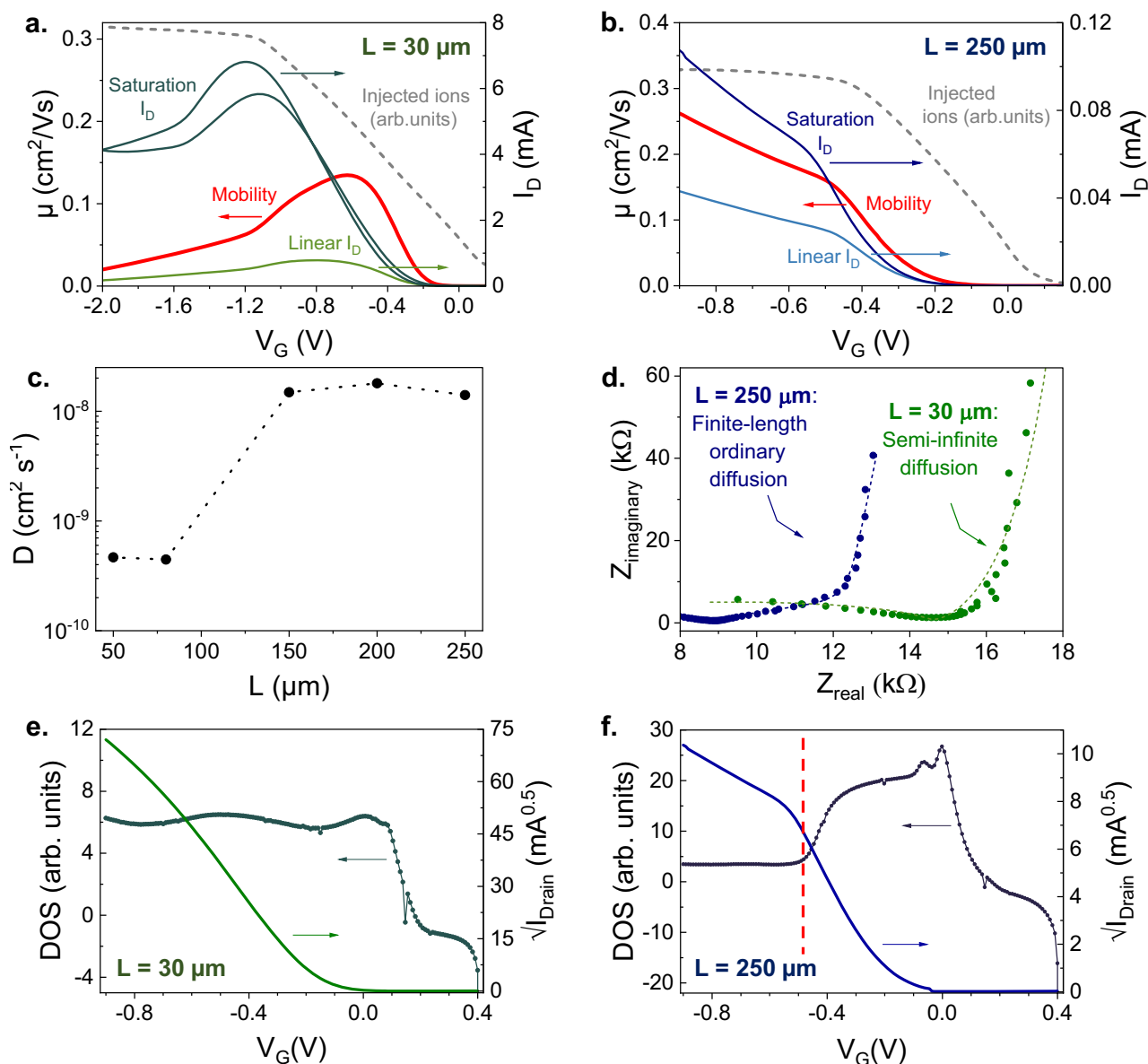


Fig. 3 | Channel geometry determines whether an organic electrochemical transistor channel is volumetric or at the interphase. Charge carrier mobility (μ), injected ions (Q_{injected}), linear drain current (I_D), and saturation I_D as a function of gate voltage (V_G) for channel lengths (L) $L = 30 \mu\text{m}$ and $L = 250 \mu\text{m}$. Here, **a** shows that, for the small channel, $L = 30 \mu\text{m}$, a soft Coulomb gap is formed at $V_G \approx -0.6 \text{ V}$, whereas **b** shows that, for the large channel, a hard Coulomb gap is formed at $V_G \approx -0.5 \text{ V}$. In both (**a**, **b**), μ and linear I_D were measured at drain voltage (V_D) = -0.1 V , and saturation I_D was measured at $V_D = -0.9 \text{ V}$. **c** Diffusion coefficient (D) as a function of L at fixed potential (V), equivalent to the gate voltage ($-V_G$), where $V_G = -0.75 \text{ V}$. D was obtained from EIS for channels with $L = 50, 80, 150, 200$,

and $250 \mu\text{m}$, and the channel width fixed at $500 \mu\text{m}$. **d** EIS data Nyquist plots for $L = 30 \mu\text{m}$ and $L = 250 \mu\text{m}$. The measured data is represented by symbols, and the solid lines show the circuit model fits, which use different Warburg elements as shown in Fig. S14, and indicate different ion distribution within the channels depending on the length. **e** Density of states (DOS) and $\sqrt{I_D}$, both as a function of V_G , for $L = 30 \mu\text{m}$. **f** DOS and $\sqrt{I_D}$, both as a function of V_G , for $L = 250 \mu\text{m}$. The dashed line shows the direct relationship between the kink in $\sqrt{I_D}$ and change in the DOS, and indicates the formation of the hard Coulomb gap at $V_G \approx -0.5 \text{ V}$. All OECTs are made from pT2gTT and use BMIMPF₆⁻ as an electrolyte. $\sqrt{I_D}$ was measured at $V_D = -0.9 \text{ V}$.

$4.6 \times 10^{-10} \text{ cm}^2 \text{ s}^{-1}$ for the smaller channel lengths ($L = 50 \mu\text{m}$ and $80 \mu\text{m}$). Additionally, a change in diffusion and impedance is observed in the largest channels ($\approx 95\%$ change in D with V_G for $L = 250 \mu\text{m}$), but not in the smallest channels ($\approx 0.12\%$ change in D with V_G for $L = 50 \mu\text{m}$). Namely, for the largest channels, Supplementary Video S1 shows how the diffusion-related part in EIS data (identified as Region 2 in Fig. S14 in the Supplementary Data, and discussed in Supplementary Equations and Discussion) initially decreases in impedance as V increases. The impedance then starts to increase again, and this change happens at the same voltage that we observe the kink and the change in Q_{injected} (Fig. 2d, e). For the small channels, however, Supplementary Video S2 shows an initial, minor decrease in impedance as V increases, and at $V = 0.3 \text{ V}$, the impedance is fixed. The observation that OECT channel dimensions significantly impact I_D is important because it is a violation of the Bernards and Malliaras model that has not been identified before.

Yet, the most remarkable observation from the EIS data is from the Warburg element fittings, which suggest stark differences in how the ions are distributed in the channel depending on the channel length. Specifically, it is not possible to fit the smallest channel $30 \mu\text{m}$ channel size with a circuit model incorporating a finite length ordinary diffusion (FLOD) Warburg element^{53,54} at constant V . Indeed, Figs. 3d and S15b show the smallest channel, $L = 30 \mu\text{m}$, can only be fitted using a semi-infinite diffusion Warburg element, which indicates that the ions in the channel are closer to the electrolyte/OMIEC interphase. The latter is because semi-infinite diffusion fits are used when the range over which the ion concentration gradient changes is significantly smaller than the thickness of the bulk material (see Supplementary Equations and Discussion)^{55,56}. In stark contrast, Fig. S15a shows that the EIS data for $L = 250 \mu\text{m}$ is accurately fitted with a FLOD Warburg element, indicating that the large channel has formed, comparatively, further within the bulk or volumetrically. These findings are also supported by literature discussing OECTs that operate with either dominant volumetric effects or electrostatic double layer effects^{28, 57, 58}. While microstructure³⁷, ionic species⁵⁸, low ionic mobility, and OMIEC/electrolyte injection barriers²⁸ can determine how the conductive channel forms, no reports to date have examined the role of channel dimension on whether an OECT channel forms volumetrically or at the OMIEC/electrolyte interphase.

For a physical explanation as to why I_D and μ are markedly different in OECTs with large and small channel lengths, we used DCM to measure the DOS (Fig. 3e, f), as the Fermi level moves toward the highest occupied molecular orbital (HOMO) with increasing V_G ⁴⁸. First, it is surprising that the drop off in μ at $V_G \approx -0.6 \text{ V}$ (Fig. S12c) for the small channel ($L = 30 \mu\text{m}$) is not reflected in the saturation current, I_D . Namely, a drop off in μ is associated with the formation of a soft Coulomb gap in the DOS, from partial localization of electronic charge carriers causing the HOMO to split into two bands; it has been shown previously that this phenomenon corresponds with decreasing current^{59,60}. One possibility is that the effective voltage is greater in the saturation regime ($V_D = -0.9 \text{ V}$), and the soft gap is small enough for carriers to cross with the additional energy. This hypothesis is supported by the drop off in μ corresponding with a change in I_D in the linear regime ($V_D = -0.1 \text{ V}$) (Fig. 3a), where the channel effective voltage is low, and the carriers cannot pass the soft bandgap. Then, once the hole-hole and ion-hole interactions are significant enough to form a hard gap at $V_G \approx -1.1 \text{ V}$, there is a drop off in saturation I_D , as well as a further change in μ and linear I_D (Fig. 3a); that is to say, a large Coulomb gap has formed in the DOS that shuts down conductance, and stops sub-band filling^{59,60}. In further support of the formation of a soft gap at $V_G \approx -0.6 \text{ V}$ and a hard gap at $V_G \approx -1.1 \text{ V}$ is the fact that the small channel forms closer to the OMIEC/electrolyte interphase, where hole-hole Coulombic interactions are more significant because of the relatively higher areal charge density⁶¹, and ion-hole Coulombic interactions are less. Specifically, a soft gap forms first because hole-hole interactions begin to localize

charge carriers, but ion-hole interactions are not yet great enough to form the hard gap. Moreover, the formation of a hard gap at $V_G \approx -1.1 \text{ V}$ is consistent with the abrupt change in Q_{injected} (Fig. 3a)—and therefore the kink in $\sqrt{I_D}$ —occurring at the same voltage: When Coulombic force is incorporated and the Nernst-Planck equation, the interactions will increase enough to suppress diffusion and cause a change in the rate with which the ions diffuse.

Finally, Fig. 3f shows that a sharp change in the DOS occurs at the same voltage as the change in Q_{injected} , and kink in $\sqrt{I_D}$ (Fig. 3b), in the large channel ($L = 250 \mu\text{m}$). Similarly, Fig. S16 shows a sharp change in the DOS occurs for the small channel ($L = 30 \mu\text{m}$) when measured at the extended V_G -range (see Fig. 2f, g), at the point in which there is a change in Q_{injected} and the kink in $\sqrt{I_D}$ appears. For the larger channel in Fig. 3b, f, in contrast to the small channel, it is surprising that μ and I_D continue to increase—albeit at a lesser rate—despite the abrupt change in the DOS. The distribution of ions within the channel may again explain this unexpected behavior. Namely, for $L = 250 \mu\text{m}$, ions are distributed throughout the volume of the channel, where there is a higher probability of hole-hole and ion-hole Coulombic interactions to cause localization and, subsequently, a hard gap leading to the sharp change in the DOS^{59,61}. While the Coulomb gap makes it more difficult for the carriers to get into available states, there is a much higher effective voltage in the large channel. Multiple trap and release and band filling models therefore make the increase in μ and I_D as a function of V_G (shown in Fig. 3b), feasible after the Coulomb gap and change in DOS (Fig. 3f): A greater effective voltage reduces E_A of the localized states, pre-fills low-lying localized states to move the Fermi level across the gap, and gives additional energy that enables localized charge carriers to move into the empty, lower HOMO. Overall, both small and large channels indicate the signature kink in $\sqrt{I_D}$ in OECTs is caused by a change in the rate with which ions diffuse into the channel, which we have also found to coincide with the formation of a hard Coulomb gap in the DOS.

Discussion

While OECTs are used to measure and compare organic mixed ionic-electronic conductor FOM, the μ and the μC^* product are being overestimated by significant differences between experimental OECT data and OECT data predicted by the Bernards and Malliaras model. The signature of an overestimated μC^* product measured from OECTs is a non-linearity or “kink” in the square root of the saturation drain current. Here, by using Fick’s second law of diffusion, we identify the origin of the kink as a change in the rate with which ions diffuse into the channel, and a concurrent formation of a hard gap in the DOS, from increased Coulombic interactions that cause carrier localization. We also find that the lateral electric field has a surprising impact on the vertical drift and accumulation of the ionic charges. The latter observation suggests a sequence of mechanisms must occur for this particular polymer/electrolyte OECT system to switch on: First, holes are injected from the source and drift into the polymer and second, anions drift into the channel. Finally, we identify parasitic channel effects in OECTs as a previously unreported violation of the Bernards and Malliaras model. Specifically, when the channel length is large, the ions are found to be better distributed throughout the volume of the polymer. Comparatively, when the length is small, the conductive channel is formed closer towards the interphase between the polymer and electrolyte. Overall, we have identified diverse, fundamental charge transport phenomena that will be crucial for enabling the realization of the remarkably broad organic mixed conductor application space.

Methods

Organic mixed ionic-electronic conductor solution and thin-film preparation

Poly[(3,6-bis(triethyleneglycolmonomethylether)thieno[2,3]thiophene-co-thiophene) (pT2gTT) was synthesized according to a previously reported procedure and was used as received; the

characterization of the received material matched that reported in ref. 18. The polymer solution was prepared at a concentration of 10 mg/mL in degassed chloroform, and spin-coated onto patterned OECT substrates in two steps: (1) 500 rpm for 5 s, and (2) 700 rpm for 45 s. The chloroform was purchased from VWR and degassed using the freeze-pump-thaw method.

Organic electrochemical transistors

Borofloat glass substrates were cleaned in an ultrasonic bath for 10 min each in the following solutions: Decon-90 soap; deionized water; acetone, and isopropanol. Substrates were dried with nitrogen gun and treated with UV Ozone for 15 min. A 10 nm chromium adhesion layer was then evaporated onto the substrates, followed by 100 nm of gold, using an Angstrom evaporator, to form the source and drain electrodes. UV Ozone and oxygen plasma treatments were then used to enhance adhesion between the substrate for a subsequent 2 μm layer of Parylene C, that was deposited using an SCS Labcoater 2010 system. Two layers of a 4% microsoap solution were spin-coated at 6000 rpm on top of the Parylene C to facilitate the removal of a second layer of Parylene C, that was deposited at a thickness of 4 μm , to act as a sacrificial layer to pattern the OECT channels. Photolithography was then used to pattern the OECT channels by exposing the SPR 220-7 photoresist to UV light with a Suss MA6 Contact Aligner, before developing with MF-26. The channels—which varied in length from 30 to 250 μm , with a fixed width of 500 μm —were then etched with oxygen, using March reactive ion etching (RIE) apparatus. The polymer solution was deposited as described above, and the upper, sacrificial layer of Parylene C layer was then peeled off to pattern with polymer with the given channel dimensions. OECT current-voltage characteristics were measured in ambient conditions, as well as under a vacuum, using a Keysight B2912B Precision Source/Measure Unit. A 500 \times 500 μm gold electrode coated with pT2gTT was used as the gate electrode (Fig. 2a). The OECT electrolytes used in this study were ionic liquids purchased from Sigma Aldrich, where BMIMBF₄ and BMIMPF₆ were purchased at >97% purity, whereas the BMIMOTf was >95% purity.

Density functional theory

Density functional theory (DFT) calculations were performed with the wB97XD functional and the 6-31g(d) basis set using Gaussian 16 Rev. A.03 software suite⁶². The geometries of BF₄⁻, PF₆⁻, and OTf⁻ were optimized with a charge of -1 and spin multiplicity of 1. The optimized geometries were then used to estimate the ion dimensions from the bond lengths and the van der Waals radii of the terminal nuclei F (1.47 Å) and O (1.52 Å). The ionic volume was calculated from the ion dimensions and ion shape as shown in Fig. 1a–c.

Activation energy measurements

OECT activation energy (E_A) was measured using temperature-dependent measurements, with a Lakeshore CPX cryostation, under vacuum, and in the saturation regime with the drain voltage set to $V_D = -1\text{ V}$. The temperature ranges for the different ionic liquids were: 300–350 K for BMIMOTf; 286–320 K for BMIMPF₆; 227–321 K for BMIMBF₄. Here, the lowest temperatures were selected to prevent the various ionic liquids from freezing. The gate voltage was swept from 0.2 to -1 V, at a scan rate of 39 mV/s. The logarithm of the drain current was plotted against 1000/T and fit with a straight line for each gate voltage. From these linear fits, E_A was found for each gate voltage using the slope of the fitted line, and following Eq. 1.

Electrochemical impedance spectroscopy

Diffusion coefficients were measured on OECTs with different channel lengths using EIS in ambient conditions, with BMIMPF₆ as the electrolyte. A platinum wire as the counter electrode, a 500 \times 500 μm gold electrode coated with pT2gTT as the reference electrode, and the

source and drain electrodes were shorted and both connected to the working terminal of an Autolab potentiostat, to act as the working electrode. The data was acquired by superimposing a 10 mV sinusoidal potential onto the DC potential ($V = -V_G$) at the working electrode (i.e., the source/drain), and across frequencies ranging from 50 kHz to 2 Hz. The DC potential was increased in 0.1 V steps from 0.1 to 0.9 V, with additional measurements made at 0.85 V and 0.75 V. Each DC potential was maintained for 20 seconds before the frequency scan was initiated. Finally, Metrohm Autolab NOVA software was used for the EIS data fitting.

Displacement current method

The displacement current, i.e., the current between the gate and source electrodes, or I_{Gate} , was measured using a Keysight B2912B Precision Source/Measure Unit. Both the source and drain electrodes were grounded, and the gate electrode was a 500 \times 500 μm gold electrode coated with pT2gTT. The gate voltage was scanned at a constant rate (v) of $v = 11\text{ mV/s}$, from 0.4 to -0.9 V, while I_{Gate} was measured. BMIMPF₆ was used as the electrolyte and the measurements were carried out under vacuum. Following each displacement current measurement, the transfer characteristics for each channel were recorded using the same voltage range and sweep rate; the drain voltage was -0.1 V for linear regime, and -0.9 V for the saturation regime. For the displacement current method experiments where the gate voltage range has extended in the small channel (length = 30 μm , Fig. 2f, g), the saturation drain voltage was kept at -0.9 V, the gate voltage was extended to -2 V, and $v = 20\text{ mV/s}$.

Data availability

All source files and experimental datasets underlying the figures in the main text and the Supplementary Information will be available via Figshare on publication with DOI of 10.6084/m9.figshare.30657443. Additional materials related to this study can be provided by the authors upon request.

References

1. Kawahara, J. et al. Fast-switching printed organic electrochemical transistors including electronic vias through plastic and paper substrates. *IEEE Trans. Electron Devices* **60**, 2052–2056 (2013).
2. Kim, H. et al. Organic mixed ionic–electronic conductors for bioelectronic sensors: materials and operation mechanisms. *Adv. Sci.* **11**, 2306191 (2024).
3. Hütter, P. C. et al. All screen-printed logic gates based on organic electrochemical transistors. *IEEE Trans. Electron Devices* **62**, 4231–4236 (2015).
4. Barbosa, H. F.dP. et al. Processing of organic electrochemical transistors. *MRS Commun.* **14**, 132–148 (2024).
5. Andersson Ersman, P. et al. Screen printed digital circuits based on vertical organic electrochemical transistors. *Flex. Print. Electron.* **2**, 045008 (2017).
6. Afonso, M., Morgado, J. & Alcácer, L. Inkjet printed organic electrochemical transistors with highly conducting polymer electrolytes. *J. Appl. Phys.* **120**, 165502 (2016).
7. Shahi, M. et al. The organic electrochemical transistor conundrum when reporting a mixed ionic–electronic transport figure of merit. *Nat. Mater.* **23**, 2–8 (2024).
8. Paudel, P. R. et al. The transient response of organic electrochemical transistors. *Adv. Theory Simul.* **5**, 2100563 (2022).
9. Bitton, S. & Tessler, N. Unveiling the impact of the electrolyte's counter ions on organic electrochemical transistor performance. *Adv. Electron. Mater.* **10**, 2300766 (2024).
10. Tu, D. & Fabiano, S. Mixed ion–electron transport in organic electrochemical transistors. *Appl. Phys. Lett.* **117**, 080501 (2020).
11. Prigodin, V. N. et al. Electron-ion interaction in doped conducting polymers. *Phys. Rev. B* **78**, 035203 (2008).

12. Paudel, P. R. et al. Organic electrochemical transistors – from device models to a targeted design of materials. *J. Mater. Chem. C* **9**, 9761–9790 (2021).
13. Paterson, A. F. et al. Recent progress in high-mobility organic transistors: a reality check. *Adv. Mater.* **30**, 1801079 (2018).
14. Choi, H. H. et al. Critical assessment of charge mobility extraction in FETs. *Nat. Mater.* **17**, 2–7 (2018).
15. McCulloch, I., Salleo, A. & Chabinyc, M. Avoid the kinks when measuring mobility. *Science* **352**, 1521–1522 (2016).
16. Vanoni, C., Tsujino, S. & Jung, T. A. Reduction of the contact resistance by doping in pentacene few monolayers thin film transistors and self-assembled nanocrystals. *Appl. Phys. Lett.* **90**, 193119 (2007).
17. Schafer, E. A. et al. Sources and mechanism of degradation in p-type thiophene-based organic electrochemical transistors. *ACS Appl. Electron. Mater.* **4**, 1391–1404 (2022).
18. Ding, B. et al. Development of synthetically accessible glycolated polythiophenes for high-performance organic electrochemical transistors. *Adv. Electron. Mater.* **10**, 2300580 (2024).
19. Tjhe, D. H. L. et al. Non-equilibrium transport in polymer mixed ionic–electronic conductors at ultrahigh charge densities. *Nat. Mater.* **23**, 1712–1719 (2024).
20. Wu, X. et al. Ionic-liquid induced morphology tuning of PEDOT:PSS for high-performance organic electrochemical transistors. *Adv. Funct. Mater.* **32**, 2108510 (2022).
21. Bongartz, L. M. et al. Bistable organic electrochemical transistors: enthalpy vs. entropy. *Nat. Commun.* **15**, 6819 (2024).
22. Keene, S. T. et al. Hole-limited electrochemical doping in conjugated polymers. *Nat. Mater.* **22**, 1121–1127 (2023).
23. Giannini, S. & Blumberger, J. Charge transport in organic semiconductors: the perspective from nonadiabatic molecular dynamics. *Acc. Chem. Res.* **55**, 819–830 (2022).
24. Karl, N. Charge carrier transport in organic semiconductors. *Synth. Met.* **133–134**, 649–657 (2003).
25. Coppedè, N., Villani, M. & Gentile, F. Diffusion driven selectivity in organic electrochemical transistors. *Sci. Rep.* **4**, 4297 (2014).
26. Tseng, H. et al. Membrane-free, selective ion sensing by combining organic electrochemical transistors and impedance analysis of ionic diffusion. *ACS Appl. Electron. Mater.* **3**, 3898–3903 (2021).
27. Szymański, M. Z., Tu, D. & Forchheimer, R. 2-D drift-diffusion simulation of organic electrochemical transistors. *IEEE Trans. Electron Devices* **64**, 5114–5120 (2017).
28. Ohayon, D., Druet, V. & Inal, S. A guide for the characterization of organic electrochemical transistors and channel materials. *Chem. Soc. Rev.* **52**, 1001–1023 (2023).
29. Braga, D. et al. Ultralow contact resistance in electrolyte-gated organic thin film transistors. *Appl. Phys. Lett.* **97**, 193311 (2010).
30. Bernards, D. & Malliaras, G. Steady-state and transient behavior of organic electrochemical transistors. *Adv. Funct. Mater.* **17**, 3538 (2007).
31. Mabeck, J. T. et al. Microfluidic gating of an organic electrochemical transistor. *Appl. Phys. Lett.* **87**, 013503 (2005).
32. Toss, H. et al. On the mode of operation in electrolyte-gated thin film transistors based on different substituted polythiophenes. *Org. Electron.* **15**, 2420–2427 (2014).
33. Savva, A. et al. Balancing ionic and electronic conduction for high-performance organic electrochemical transistors. *Adv. Funct. Mater.* **30**, 1907657 (2020).
34. Savva, A. et al. Influence of water on the performance of organic electrochemical transistors. *Chem. Mater.* **31**, 927–937 (2019).
35. Jia, H. et al. Engineering donor–acceptor conjugated polymers for high-performance and fast-response organic electrochemical transistors. *J. Mater. Chem. C* **9**, 4927–4934 (2021).
36. Andersson Ersman, P. et al. Fast-switching all-printed organic electrochemical transistors. *Org. Electron.* **14**, 1276–1280 (2013).
37. Campana, A. et al. Electrocardiographic recording with conformable organic electrochemical transistor fabricated on resorbable bioscaffold. *Adv. Mater.* **26**, 3874–3878 (2014).
38. Rivnay, J. et al. High-performance transistors for bioelectronics through tuning of channel thickness. *Sci. Adv.* **1**, e1400251 (2015).
39. Spyropoulos, G. D., Gelinias, J. N. & Khodagholy, D. Internal ion-gated organic electrochemical transistor: a building block for integrated bioelectronics. *Sci. Adv.* **5**, eaau7378 (2019).
40. Cea, C. et al. Enhancement-mode ion-based transistor as a comprehensive interface and real-time processing unit for in vivo electrophysiology. *Nat. Mater.* **19**, 679–686 (2020).
41. Kaphle, V. et al. Finding the equilibrium of organic electrochemical transistors. *Nat. Commun.* **11**, 2515 (2020).
42. Shirinskaya, A. et al. Numerical modeling of an organic electrochemical transistor. *Biosensors* **8**, <https://doi.org/10.3390/bios8040103> (2018).
43. Pang, M.-C. et al. Mechanical behaviour of inorganic solid-state batteries: can we model the ionic mobility in the electrolyte with Nernst–Einstein’s relation? *Phys. Chem. Chem. Phys.* **23**, 27159–27170 (2021).
44. Paul, A. et al. Fick’s laws of diffusion. in *Thermodynamics, Diffusion and the Kirkendall Effect in Solids*, (eds Paul, A. et al.) 115–139 (Springer International Publishing, 2014).
45. Wilkinson, D. S., Mass transport in solids and fluids. In *Cambridge Solid State Science Series* (Cambridge University Press, 2000).
46. Marková, A. et al. Serial resistance effect on organic electrochemical transistors’ transconductance. *IEEE Sens. J.* **23**, 19417–19423 (2023).
47. Xie, W. & Frisbie, C. D. Organic electrical double layer transistors based on rubrene single crystals: examining transport at high surface charge densities above 10^{13} cm^{-2} . *J. Phys. Chem. C* **115**, 14360–14368 (2011).
48. Paulsen, B. D. & Frisbie, C. D. Dependence of conductivity on charge density and electrochemical potential in polymer semiconductors gated with ionic liquids. *J. Phys. Chem. C* **116**, 3132–3141 (2012).
49. Baustert, K. N. et al. Combination of counterion size and doping concentration determines the electronic and thermoelectric properties of semiconducting polymers. *Adv. Mater.* **36**, 2313863 (2024).
50. Aubry, T. J. et al. Dodecaborane-based dopants designed to shield anion electrostatics lead to increased carrier mobility in a doped conjugated polymer. *Adv. Mater.* **31**, 1805647 (2019).
51. Jacobs, I. E. et al. Structural and dynamic disorder, not ionic trapping, controls charge transport in highly doped conducting polymers. *J. Am. Chem. Soc.* **144**, 3005–3019 (2022).
52. Friedlein, J. T., McLeod, R. R. & Rivnay, J. Device physics of organic electrochemical transistors. *Org. Electron.* **63**, 398–414 (2018).
53. Harris, J. K. & Ratcliff, E. L. Ion diffusion coefficients in poly(3-alkylthiophenes) for energy conversion and biosensing: role of side-chain length and microstructure. *J. Mater. Chem. C* **8**, 13319–13327 (2020).
54. Basri, N. H. et al. Energy and power of supercapacitor using carbon electrode deposited with nanoparticles nickel oxide. *Int. J. Electrochem. Sci.* **11**, 95–110 (2016).
55. Lazanas, A. C. & Prodromidis, M. I. Electrochemical impedance spectroscopy—a tutorial. *ACS Meas. Sci. Au* **3**, 162–193 (2023).
56. Tanguy, J. et al. Poly(3-alkylthiophenes) and poly(4,4′-dialkyl-2,2′-bithiophenes): a comparative study by impedance spectroscopy and cyclic voltammetry. *Synth. Met.* **45**, 81–105 (1991).
57. Skowrons, M. et al. Depletion type organic electrochemical transistors and the gradual channel approximation. *Adv. Funct. Mater.* **34**, 2303324 (2024).
58. Teng, X. et al. Ion effects on salt-in-water electrolyte gated polymer electrochemical transistors. *Org. Electron.* **120**, 106859 (2023).

59. He, T. & Frisbie, C. D. Sub-band filling, mott-like transitions, and ion size effects in C60 single crystal electric double layer transistors. *ACS Nano* **16**, 4823–4830 (2022).
60. Frisbie, C. D. Crossing the Coulomb gap in semiconducting polymers. *Nat. Mater.* **23**, 1615–1617 (2024).
61. Cho, K. G. et al. Sub-band filling and hole transport in polythiophene-based electrolyte-gated transistors: effect of side-chain length and density. *Adv. Funct. Mater.* **33**, 2303700 (2023).
62. Frisch, M. J. et al. Gaussian 16 Rev. A.03. (Wallingford, CT., 2016).

Acknowledgements

M.S., V.N.L., P.A.E., and A.F.P. thank the National Science Foundation (NSF) through cooperative agreement numbers 2349830 and 1849213 for financial support, and (DARPA) through grant number D24AP00298-01. J.H.B. and C.R. gratefully acknowledge support from the National Science Foundation through award number 1905734 and NSF through agreement number 2349830. Computing resources on the Lipscomb High Performance Computing Cluster were provided by the University of Kentucky Centre for Computational Sciences and Information Technology Services Research Computing. B.D. acknowledges PhD funding via the President's PhD Scholarship Scheme. M.H. thanks the Royal Society for support. The authors thank Professor John Labram (University College London) and Professor Dean DeLongchamp (National Institute of Standards and Technology) for their thoughtful and insightful discussions.

Author contributions

M.S. designed the experiments, fabricated and characterized the OECTs, and analyzed the data. V.N.L. and P.A.E. carried out photolithography. J.H.B. carried out the DFT analysis with input from C.R. B.D. synthesized the BD2040 polymer with input from M. H. A.F.P. and M.S. wrote the manuscript with input from all other authors, and input from discussions with J.H.B. and C.R. A.F.P. conceived the idea, designed the experiments, and conceptualized, supervised and directed the study.

Competing interests

The authors declare no competing interests.

Additional information

Supplementary information The online version contains supplementary material available at <https://doi.org/10.1038/s41467-025-67546-2>.

Correspondence and requests for materials should be addressed to Alexandra F. Paterson.

Peer review information *Nature Communications* thanks the anonymous reviewers for their contribution to the peer review of this work. A peer review file is available.

Reprints and permissions information is available at <http://www.nature.com/reprints>

Publisher's note Springer Nature remains neutral with regard to jurisdictional claims in published maps and institutional affiliations.

Open Access This article is licensed under a Creative Commons Attribution-NonCommercial-NoDerivatives 4.0 International License, which permits any non-commercial use, sharing, distribution and reproduction in any medium or format, as long as you give appropriate credit to the original author(s) and the source, provide a link to the Creative Commons licence, and indicate if you modified the licensed material. You do not have permission under this licence to share adapted material derived from this article or parts of it. The images or other third party material in this article are included in the article's Creative Commons licence, unless indicated otherwise in a credit line to the material. If material is not included in the article's Creative Commons licence and your intended use is not permitted by statutory regulation or exceeds the permitted use, you will need to obtain permission directly from the copyright holder. To view a copy of this licence, visit <http://creativecommons.org/licenses/by-nc-nd/4.0/>.

© The Author(s) 2026